Catal Lett (2007) 119:209–216
DOI 10.1007/s10562-007-9236-0

Support Dependence of MeOH Decomposition Over Size-Selected Pt Nanoparticles

Jason R. Croy · Simon Mostafa · Jing Liu · Yongho Sohn · Helge Heinrich · Beatriz Roldan Cuenya

Received: 1 July 2007 / Accepted: 30 July 2007 / Published online: 15 August 2007

Abstract We present here the decomposition of methanol over Pt nanoparticles supported on a series of oxide powders. The samples tested may be roughly grouped in two categories consisting of large (~15–18 nm) and small (~8–9 nm) Pt particles deposited on *reducible* (CeO_2, TiO_2) and *non-reducible* (SiO_2, ZrO_2, Al_2O_3) supports. The smallest particles (~8 nm), deposited on ZrO_2, were found to be cationic and the most active for the decomposition of methanol. Furthermore, the stability of metallic Pt and its oxides was observed to be dependent on the choice of support. In all Pt containing samples the reaction proceeds via he direct decomposition of methanol, as no significant amounts of by-products were detected in the experimental range of 100–300 °C.

Keywords Pt nanoparticles · Oxide supports · Methanol · CeO_2 · TiO_2 · ZrO_2 · SiO_2 · Al_2O_3 · XPS · AFM · TEM · Mass flow reactor

1 Introduction

Methanol (MeOH) as a chemical commodity has become a staple of the modern world. Consequently, the synthesis of MeOH has long been an important topic and there is today a preferred catalytic system in wide-spread industrial use ($Cu/ZnO/Al_2O_3$) [1]. In the reverse direction, the decomposition of MeOH has increased in significance due to its applicability as a storage fuel for hydrogen and subsequent use in fuel cells. In addition, methanol's adaptability to the existing infrastructure (i.e. as a liquid fuel) makes the direct methanol fuel cell (DMFC) an attractive technology for transportation applications [2]. There are several decomposition processes currently in use and under study including direct decomposition, steam reforming, and oxidation [3]. These processes require the use of metallic nanoparticle catalysts such as Cu, Pt, and Pd supported on various oxides [4]. However, because a fundamental knowledge of these processes is still lacking, MeOH decomposition and combustion are still subjects of intense studies [5], as is the interaction of MeOH with surfaces relevant to electro-oxidation for fuel cell technologies [6–10].

There is a current debate in the literature on whether metallic Pt or Pt oxides are the most catalytically active species. As an example, PtO_2(1 1 0) surfaces have been found more reactive than metallic Pt for CO oxidation [11]. Dam al. [12] have shown that Pt dissolution in fuel cells reaches a saturation level due to the presence of a protective platinum oxide layer, and Hull et al. [13] showed enhanced activity for Pt–carbon nanotube catalysts, where the Pt particles are covered by a thin PtOx shell. On the other hand, the temporal decay in the performance of Pt-based fuel cell electrodes has been attributed to the formation of PtO and Pt dissolution [14].

In a previous work [15], we have shown that Pt nanoparticles supported on anatase TiO_2 have a size-dependent activity in the decomposition of MeOH, where an increase in activity was associated with a decrease in particle size. Furthermore, the oxidation state of the nanoparticles depended on the initial size of the particles. Although support related effects were not considered, owing to the

J. R. Croy · S. Mostafa · H. Heinrich · B. R. Cuenya (✉)
Department of Physics, University of Central Florida, Orlando, FL 32816, USA
e-mail: roldan@physics.ucf.edu

J. Liu · Y. Sohn · H. Heinrich
Center of Advanced Materials Processing and Characterization, University of Central Florida, Orlando, FL 32816, USA

use of a common support, they were assumed to be present and are in need of consideration. For example, reactive sites are expected to be present at the nanoparticle's perimeter associated with atoms in contact with the support [16, 17] and at the support itself [18, 19]. Metal–support interactions are also responsible for varying degrees of encapsulation of metallic particles in several oxide systems [20–24], and it has been shown that the acidity of the support plays a major role in the electronic state of the supported particles and thus can influence catalytic performance [25].

Although the smallest particles in the current study are relatively large (~8 nm), it will be shown that metal–support interactions are still important, especially in connection with particle oxidation state and stability against coarsening.

2 Experimental

Non-polar/polar diblock copolymers [poly(styrene)-block-poly(2vinylpyridine), Polymer Source Inc.] were dissolved in a non-polar solvent (toluene) in order to obtain spherical nano-cages (inverse micelles). These micelles were then loaded with a metal salt ($H_2PtCl_6 \cdot 6H_2O$) to produce self-confined and size-selected Pt nanoparticles. The particle size was controlled by using a polymer with a specific head length [PS(27700)-PVP(4300), i.e. constant PVP molecular weight for all samples] and by tuning the metal-salt/polymer head concentration in the solution [26–28]. The solution was then mixed with a series of oxides [TiO_2(anatase), CeO_2, ZrO_2, α-Al_2O_3, and SiO_2] in the form of a powder having nominal grain sizes of in the range of 32–45 nm. All samples were calcined in air at 500 °C for 2.5 h. Each catalyst sample had a total weight of 100 mg and contained 2% by weight Pt. A metal-salt/PVP concentration ratio of 0.6 was used to create Pt nanoparticles having a narrow size distribution. The one exception was a second Pt/CeO_2 sample prepared with the same polymer, but with a metal-salt/PVP concentration of 0.2, Fig. 1. This resulted in a solution of Pt particles with a smaller average size, labeled Pt/CeO_2(#2). A second solution was desirable in the case of CeO_2-supported particles since significant nanoparticle sintering was observed in this support upon our thermal treatment.

Powder samples were deposited on carbon-coated stickers and transferred to an ultra high vacuum system (UHV, SPECS GmbH) for surface analysis by X-ray photoelectron spectroscopy (XPS). XPS data were collected using a monochromatic X-ray source (Al-Kα, 1486.6 eV) operating at 300 W and a flood gun was used to correct for surface charging during measurement. The respective binding energies of the powder samples were referenced to the Ti $2p_{3/2}$ [TiO_2] peak at 458.6 eV [29], Ce $3d_{5/2}$ [CeO_2] at 882.2 eV [30], Al $2p_{3/2}$ [Al_2O_3] at 74.5 eV [31], Si $2p_{3/2}$ [SiO_2] at 103.8 eV [32], and Zr $3d_{3/2}$ [ZrO_2] at 183.0 eV [33].

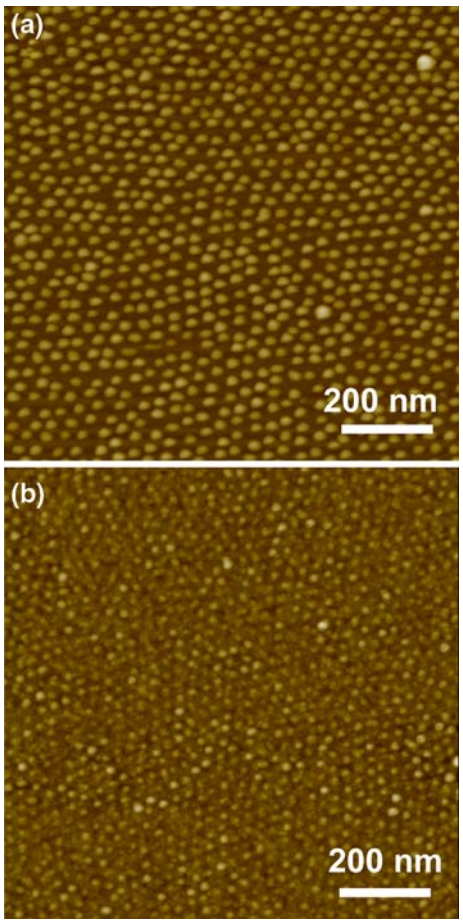

Fig. 1 Tapping mode AFM images of size-selected Pt nanoparticles dip-coated on SiO_2/Si(0 0 1) and annealed in UHV at 500 °C for 30 min. Samples were prepared using Pt/PVP concentrations of 0.6 (**a**) and 0.2 (**b**). The *z* scale is 0–20 nm for (**a**) and 0–10 nm for (**b**)

Catalytic decomposition of methanol in the vapor phase was carried out in a packed-bed mass flow reactor with a vertical quartz tube (inside diameter 4 mm) serving as the reactor vessel. In order to promote flow through the reactor, the powder catalysts (100 mg, 2 wt.% Pt) were mixed with 200 mg of inert quartz sand and divided into six 50 mg segments. These segments were separated and supported in the reactor by glass wool plugs. A thermocouple (K-type) in contact with the reactor was used to monitor temperature. Immediately prior to the reaction all catalysts were heated for one hour at ~200 °C (below the initial calcination temperatures used to remove the polymeric nanoparticle shell) in a flow of He at 10 mL/min. Activities were measured at atmospheric pressure in the range of 100–300 °C. Helium was used as the carrier gas during all reactions and regulated at 10 mL/min by a mass flow controller (MKS). The product stream of the reactor was

monitored by a quadrupole mass spectrometer (QMS, HIDEN, HPR-20) with partial pressures of the product gases measured using the system's Faraday cup and SEM detectors. The QMS inlet has a maximum consumption of 16 mL/min and several flow experiments were conducted to optimize the experimental conditions. The composition of the feed was 0.01% MeOH relative to the flow of He, as determined by the partial pressures of He and the main fragment ion of MeOH (m/q = 31).

The polymer-salt solutions were also dip-coated on SiO_2/Si(0 0 1) substrates in order to obtain particle size information (height) via atomic force microscopy (AFM) with a Nanoscope Multimode (Digital Instruments) microscope operating in tapping mode. In addition, transmission electron microscopy (TEM) was carried out on the powder samples with a Tecnai F30 TEM operating at an accelerating voltage of 300 kV.

3 Results and Discussion

3.1 Morphological and Structural Characterization

Figure 1 displays AFM images of the nanoparticle polymeric solutions dip-coated on SiO_2/Si(001) after UHV annealing for 30 min at 500 °C. Figure 1a shows the particle solution used in all samples except the Pt/CeO_2(#2) which is shown in Fig. 1b. At this temperature, removal of the encapsulating polymer is observed by monitoring the C-1s XPS signal. Analysis of the images taken after annealing gives average particle height distributions of 5.1 ± 0.6 nm for (a), and 2.7 ± 0.5 for (b).

Figures 2b–d and 3 show typical bright-field TEM images of Pt nanoparticles supported on selected oxide powders. All samples underwent the same thermal treatments as described above and were prepared using the same nanoparticle polymeric solution [except Pt/CeO_2(#2)]. Low magnification images were employed to obtain the average diameter of the Pt nanoparticles supported on the oxide powders.

Figure 2a displays a high angle annular dark field image, obtained by scanning transmission electron microscopy (STEM), of the Pt/CeO_2(#1) sample. The light-colored areas in this image correspond to Pt-rich regions. Figure 2b shows a bright field image of the same region, and Fig. 2c shows a high resolution image of a Pt particle (∼14 nm) [marked by (1) in Fig. 2b] in this sample. From Fig. 2c a lattice parameter of 3.95 ± 0.04 Å was obtained, in good agreement with literature values of 3.92 Å for fcc-Pt [34]. In Fig. 2c the nanoparticle appears faceted (typical feature of nanoparticles in this sample) and a Pt(1 1 1) terrace is observed. For this sample, the support itself (CeO_2) displays significant agglomeration after annealing in air. In addition, the average Pt particle size in this sample was 14.6 ± 2.7 nm, indicating that strong nanoparticle coarsening had occurred. One explanation for sintering could be, as given by Perrichon et al. [35], the destabilization of Pt particles on ceria. This effect stems from surface reorganization induced by O^{2-} mobility at temperatures near 300 °C, which is below our calcination temperature (500 °C). The authors also show an encapsulation/decoration effect which increases with increasing reduction temperatures with smaller particles being more susceptible to this phenomenon. This possibility will be discussed in connection with the activity of our two Pt/CeO_2 samples. Figure 2d shows a Pt particle (∼12 nm) in our sample labeled Pt/CeO_2(#2). This sample was made from a particle solution having a size distribution roughly half the size of the Pt/CeO_2(#1) sample. Analysis of the HRTEM image of a small Pt particle in this sample indicated a slightly higher value for the lattice parameter (4.0 ± 0.04). Penner et al. [36] have observed the formation of Pt-ceria alloys starting at ∼450 °C with a lattice parameter of 4.16 Å. Because this sample underwent the same thermal treatment as the Pt/CeO_2(#1) sample, and both samples show similar activities and size distributions, we might conclude that Pt particles, supported on CeO_2, are not stable at annealing temperatures of 500 °C or more, and Pt ceria alloys can be formed. In particular, smaller Pt particles seem to be more susceptible to the interaction with CeO_2, in agreement with Perrichon et al. [35]. On Ce thin films deposited on Pt foils, Tang et al. [37] found evidence of strong Ce–Pt interactions and interdiffusion (rather than encapsulation) at and above room temperature. The presence of Pt-oxides at the nanoparticle's surface could not be detected by TEM, but will be discussed in the next section based on our XPS data.

For the Pt/SiO_2 sample, Fig. 3a, a similar sintering behavior was observed. However, in this sample the distribution of particle sizes was very broad and averaged 15 ± 10 nm. This might be related to the fact that the support itself was not of nanometer scale, but rather started out as large (1/8″) pellets and was ground by hand into agglomerated powder. This may present to the supported particles a more widely distributed set of surface sites available for nucleation as compared to the already nanometer-sized ceria support. However, sintering of Pt on SiO_2 is not a new phenomenon and can be more prominent when heating takes place in air as compared to an inert atmosphere [38]. Figure 3a(inset) displays a uniform region within the Pt/SiO_2 sample.

The Pt/Al_2O_3, Fig. 3b, and Pt/ZrO_2, Fig. 3c, d, each show similar size distributions with diameters of 8.7 ± 2.1 and 8.3 ± 1.6 nm, respectively. These values are also in close proximity to the distribution of the Pt/TiO_2 sample having an average particle diameter of 8.6 ± 1.2 nm, details and images of which can be found in Ref. [15].

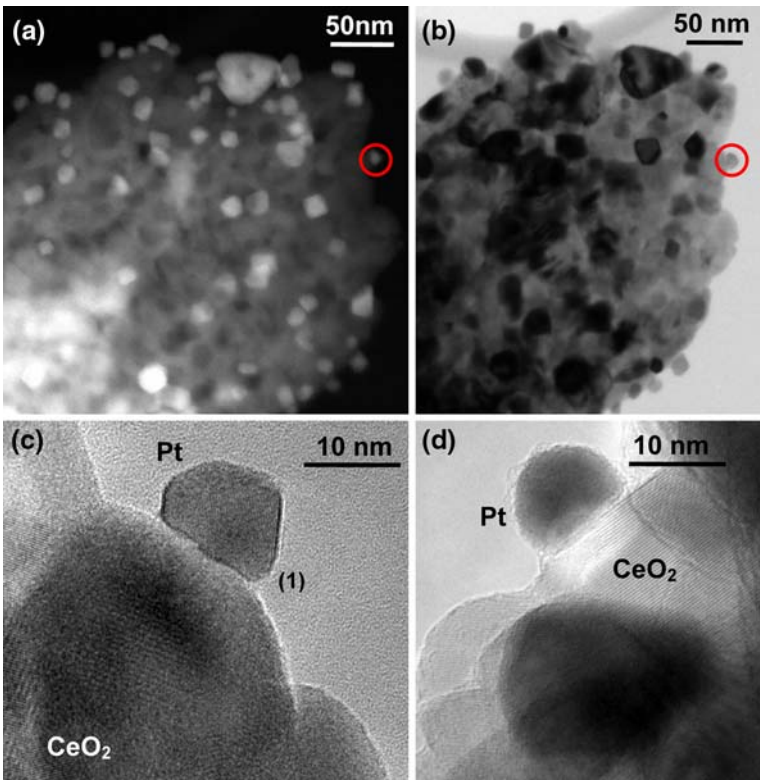

Fig. 2 Pt nanoparticles prepared by micelle encapsulation supported on CeO_2: (**a**) high angle annular dark field image obtained by scanning transmission electron microscopy (STEM) of Pt/CeO_2 (#1), (**b**) bright field image of same region as in (**a**), (**c**) high magnification image of Pt particle indicated by the circles in (**a**) and (**b**) and marked with a (1), (**d**) Pt particle on CeO_2 from Pt/CeO_2(#2) prepared initially with a solution of smaller Pt particles (Fig. 1**b**). Both samples were annealed at 500 °C

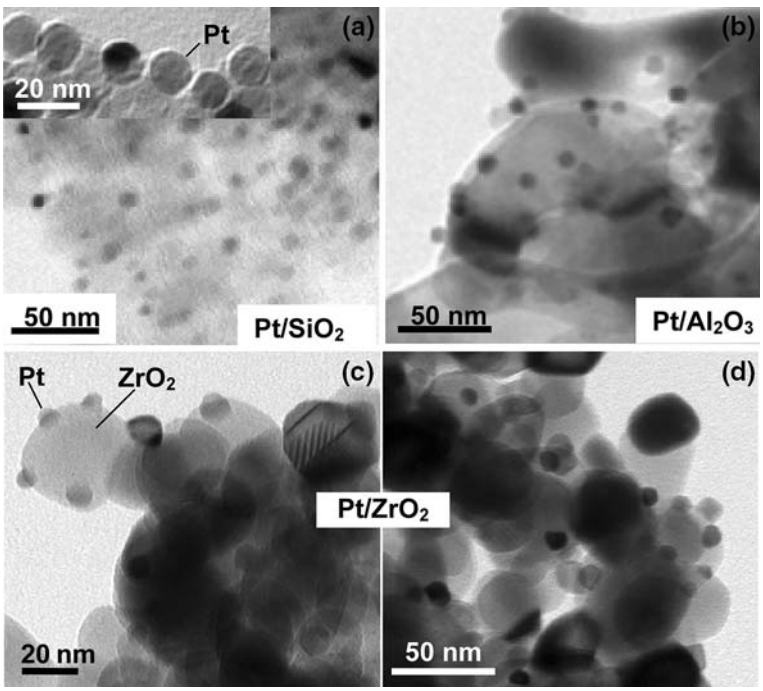

Fig. 3 Pt nanoparticles prepared by micelle encapsulation supported on selected oxide powders: (**a**) Pt/SiO_2, (**b**) Pt/Al_2O_3, (**c**)–(**d**) Pt/ZrO_2. All samples were annealed at 500 °C

3.2 Electronic and Chemical Characterization

Figure 4 shows XPS spectra of Pt deposited on the different oxide powder supports measured after annealing at 500 °C. In Fig. 4a the solid lines indicate the positions of the main core-level peaks of metallic Pt at 71.1 eV ($4f_{7/2}$) and 74.3 eV ($4f_{5/2}$), the dashed lines Pt^{2+} in PtO (73.3 and 76.6 eV), and the dotted lines Pt^{4+} in PtO_2 (75.0 and 78.8 eV). For the Pt/TiO_2 sample, we see that it is predominantly metallic with the $4f_{7/2}$ appearing at ~70.5 eV. This corresponds to a negative binding energy shift of ~0.6 eV with respect to the bulk value

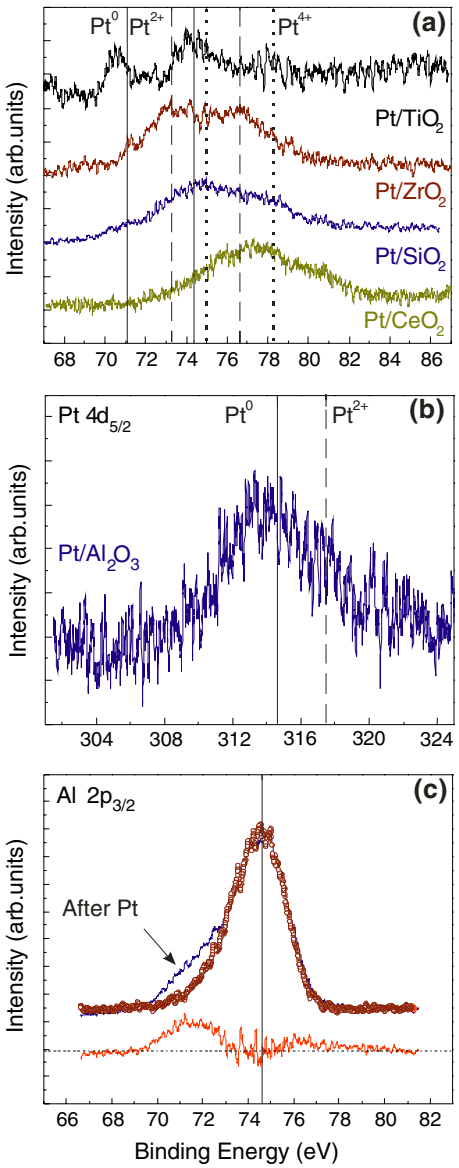

Fig. 4 (**a**) Pt-4f core level XPS spectra of Pt nanoparticles supported on: (from top to bottom) TiO_2, ZrO_2, SiO_2, CeO_2(#1). (**b**) Pt $4d_{5/2}$ from Pt/Al_2O_3. (**c**) Al $2p_{3/2}$ before and after the addition of Pt. All spectra were measured after removal of the encapsulating polymer by annealing in air at 500 °C

of 71.1 eV. This is in agreement with our previous results [15] and is close to values reported elsewhere for similar TiO_2^- supported Pt particles [39]. Such negative energy shifts can be explained by charge transfer to the particle from the support due to delocalized electron distributions arising from oxygen vacancies [40], or small particles with a large number of surface atoms having reduced coordination numbers [41]. The Pt/ZrO_2 and Pt/SiO_2 show a convolution of Pt^{2+} and Pt^{4+}, with the former being mainly Pt^{2+} and the latter slightly favoring contributions from Pt^{4+}. The Pt/CeO_2(#1) sample appears highly oxidized (mainly Pt^{4+}) and the higher binding energies indicate a strong interaction between the CeO_2 support and the Pt particles. As was mentioned before, the possible formation of Pt–Ce alloys might explain the anomalously large binding energies observed in the XPS data of these samples. For the Pt/CeO_2(#2) sample, a similar spectrum was obtained as that shown for the Pt/CeO_2(#1) sample. Tang et al. have shown shifts to higher binding energies (+0.2 eV with respect to bulk Pt) for ultrathin Ce films deposited on a metallic Pt foil [37]. In this work, the authors highlight the formation of Ce/Pt mixed layers due to enhanced interdiffusion at and above RT. In the case of our supported Pt nanoparticles, the large BE shifts observed for the Pt-4f core levels can be attributed to $Pt^{\delta+}$ species alloyed with cerium atoms upon annealing at 500 °C. Simply based on our XPS data (averaged from the sampling depth, where a Ce concentration gradient exists) we cannot conclude whether Ce atoms are at the surface of the Pt clusters (encapsulation effects) or they are surrounded by Pt atoms in intermetallic compounds. A previous work by Fu et al. [42] also discusses the possibility of Pt ion diffusion into subsurface CeO_2 layers. Interestingly, and in agreement with our results, their XPS spectra obtained on 2.5-nmlarge Pt nanoparticles supported on CeO_2 (6 nm) after calcination at 500 °C indicate the presence of Pt-oxide species, mainly Pt^{4+}.

Figure 4b shows the Pt $4d_{5/2}$ peak in the Pt/Al_2O_3 sample appearing at ~314.0 eV for Pt^0 (solid line) and ~317.5 eV for Pt^{2+} (dashed line). Here again, as in the case of Pt/TiO_2, this sample is mainly Pt^0 and shows a negative binding energy shift of ~0.6 eV as compared to the bulk value of metallic Pt at 314.6 eV. Figure 4c shows the Pt 4f region for the Pt/Al_2O_3 sample. Here the Al $2p_{3/2}$ at 74.5 eV falls in the middle of the range where we expect to see the Pt 4f peaks. Shown is a superposition of two spectra taken before and after the addition of Pt to our Al_2O_3 support. The shoulder, due to Pt, is emphasized with an arrow and the difference between the two curves (Pt contribution) is plotted at the bottom of the graph.

3.3 Catalytic Activity and Selectivity

Figure. 5 displays the activity and selectivity for the decomposition of MeOH of the different oxide powders prior to the addition of Pt. Activity is defined in terms of MeOH conversion and is given by the equation

$$\frac{P_i - P_T}{P_i} \times 100 \quad (1)$$

where P_i is the initial partial pressure of the main fragment ion of methanol (m/q = 31) and P_T is the partial pressure at a given temperature throughout the experiment.

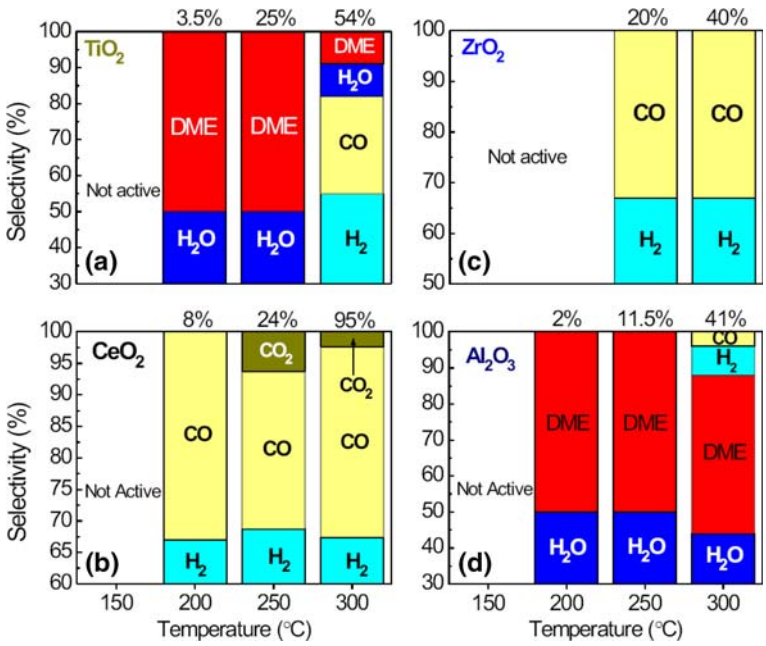

Fig. 5 Catalytic activity (conversion) and selectivity of commercial nanocrystalline oxide powders for MeOH decomposition with average grain sizes of ~32 nm for TiO_2 (**a**), ~40 nm for CeO_2 (**b**), ~45 nm for ZrO_2 (**c**), and ~35 nm for Al_2O_3 (**d**). The number across the top of each chart gives the MeOH conversion (%) at each temperature. SiO_2 (not shown) is almost completely inert, showing only ~3% MeOH conversion at 300 °C. All powders have been calcined at 500 °C for 2.5 h before the reaction

The percentages along the top of each graph represent the MeOH conversion at a particular temperature as given by Eq. (1). Selectivity for each product gas is derived from the QMS data, along with stoichiometric considerations [Eqs. (3)–(5)], and is defined as the percent of the total product that each particular partial gas pressure represents,

$$selectivity\,(\%) = \frac{A_n}{\sum A_n} \times 100 \tag{2}$$

where A_n represents the output of the nth product gas. In our experiments CO_2, and Dimethyl ether (DME) were obtained as by-products. CO_2 originates from CO produced in the decomposition of MeOH, reaction (3), and possible mechanisms involved in the production of CO_2 are the Boudouard and water gas shift reactions, (4) and (5) respectively:

$$CH_3OH = CO + 2H_2 \tag{3}$$

$$2CO = CO_2 + C \tag{4}$$

$$CO + H_2O = CO_2 + H_2 \tag{5}$$

DME may be formed according to Eq. (6).

$$2CH_3OH = CH_3OCH_3 + H_2O \tag{6}$$

We note that during the catalyst's time on-line (~7 h) we do not observe any deactivation or visible change in the catalyst and we might then rule out reaction (4) as giving a significant contribution. However, long-term deactivation studies have not yet been performed on these catalysts.

The SiO_2 support is absent in Fig. 5 because it was found to be inert over the range of temperatures used in the experiment (100–300 °C). The TiO_2 (a) and the Al_2O_3 (d) each show similar selectivity with a tendency towards the formation of DME. However, the selectivity of DME for the Al_2O_3 remains high even at 300 °C, whereas the TiO_2 shows a marked switch towards H_2 at that temperature. The ZrO_2 sample (c) remains inactive at temperatures below 200 °C and no by-products are detected up to 300 °C. For the CeO_2 sample (b), which becomes active at temperatures above 150 °C, we see a high selectivity for H_2 and ~6% for CO_2 at 250 °C decreasing to ~2% by 300 °C. The formation of CO_2 could favor catalyst lifetime since CO poisoning will be reduced. From the QMS data, Eqs. (3) and (5), and neglecting (4), it was estimated that ~20% of the CO from MeOH decomposition goes to CO_2 through the shift reaction at 250 °C. This sample also shows excellent activity relative to the other supports with almost 100% conversion at 300 °C. TiO_2 being the second most active with only 54% conversion at 300 °C. None of the supports tested were active for MeOH decomposition at or below 150 °C.

Figure 6 shows the same type of data for the supports after the addition of Pt nanoparticles. Here we show a plot of MeOH conversion (%) as a function of the reactor temperature with the dotted line denoting 50% conversion. In all of the Pt containing samples no by-products were observed in the range of temperatures tested. Therefore, the reaction proceeds by way of direct decomposition. Again, as in Fig. 5, we see similarities between the Pt/TiO_2 and

Pt/Al_2O_3 samples. Pt/TiO_2 and Pt/Al_2O_3 have similar average particle size distributions of ~8.6–8.7 nm, and show similar activity. The Pt/Al_2O_3 slightly outperforms the Pt/TiO_2 sample reaching a higher conversion at 250 °C. For the Pt/ZrO_2 sample (Pt diameter ~8.3 ± 1.6 nm) we see that it is by far the most active at low temperatures reaching 73% conversion at 200 °C. The Pt/SiO_2 (Pt diameter ~15.0 ± 10.4 nm) now becomes active above 150 °C with excellent selectivity for H_2 and ~60% conversion at 300 °C. Because the SiO_2 support was completely inactive we may attribute this activity to the addition of Pt. Although the average Pt particle size in the Pt/CeO_2(#1) sample is much larger than that on the other substrates (~14.6 ± 2.7 nm) its activity is only slightly lower than that of Pt/TiO_2 and Pt/Al_2O_3. This effect may be attributed to the relatively high MeOH conversion observed on our Pt-free nanocrystalline CeO_2 powders, and the addition of even large Pt particles further enhanced the activity. Because this support performed relatively well before the addition of Pt, and our TEM images show agglomeration on this sample (Fig. 2a, b), an additional sample was prepared with the goal of minimizing particle growth. This was done by preparing an alternate micelle solution with a Pt particle size distribution roughly half the size of the initial sample, as seen in the AFM images of Fig. 1. From here the same thermal treatment was done as on the initial sample and TEM images were taken. Unfortunately the new sample, denoted as Pt/CeO_2(#2), produced analogous reactivity results, also shown in Fig. 6. The TEM images obtained from this sample, after annealing in air at 500 °C and before the reaction, were very similar to those of the first Pt/CeO_2(#1) sample (Fig. 2) revealing considerable particle sintering.

The general order for reaching the 50% conversion mark may be listed as follows: Pt/ZrO_2, Pt/Al_2O_3, Pt/TiO_2, Pt/CeO_2, Pt/SiO_2. Surprisingly, this trend does not seem to correlate with the enhanced catalytic activity expected for nanoparticles supported on highly reducible oxides.

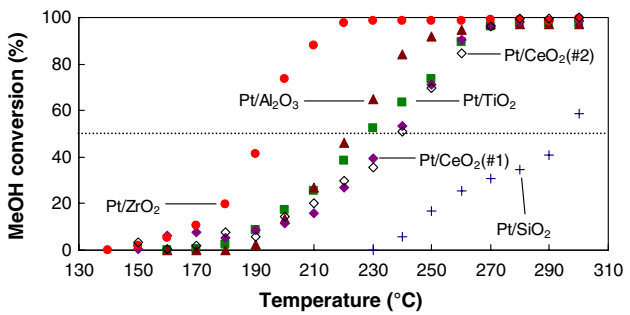

Fig. 6 MeOH decomposition over Pt nanoparticles supported on nanocrystalline oxide powders: Pt/ZrO_2 (●), Pt/Al_2O_3 (▲), Pt/TiO_2 (■), Pt/CeO_2(#1) (◆), Pt/CeO_2(#2) (◇), Pt/SiO_2 (+). All samples have been calcined at 500 °C for 2.5 h before the reaction

However, it is in agreement with Ref. [43] and results obtained by Usami et al. [44] who have shown that Pd/ZrO_2 is more active for MeOH decomposition than Pd/CeO_2, Pd/TiO_2, as well as Pd/SiO_2. In addition, the authors determined that cationic Pd was advantageous for this reaction, in agreement with the XPS data (Fig. 4) of our Pt/ZrO_2 sample.

An important point to note is that the least active samples (Pt/CeO_2 and Pt/SiO_2) both show particle coarsening with a significant increase in particle size. There are arguments which suggest that the support may be of minimal importance as long as the particles themselves have certain qualities, in particular, a high concentration of low coordinated surface sites [45]. The density of these sites increases with decreasing particle size, and therefore, we do not expect the density of such sites in the Pt/SiO_2 and Pt/CeO_2 samples to be high as compared to the other samples. With the addition of Pt, the previously inert SiO_2 displays a dramatic increase in catalytic activity. Furthermore, the CeO_2 support alone (without Pt) outperforms the Pt/SiO_2 sample (Figs. 5 and 6) and the addition of Pt to the CeO_2 support is expected to enhance its performance even further. Although this was indeed observed, the increase in activity was not as significant as in some of the other catalysts investigated, such as Pt/ZrO_2. It has been reported that the Pt in Pt/CeO_2 is the main catalytic species for the decomposition of MeOH [46]. This suggests that the relatively small improvement observed in this sample can be attributed either to the large size of the Pt particles considered, or perhaps a partial encapsulation of the Pt particles by CeO_2, also suggested in Ref. [46]. As previously discussed, the possibility of alloy formation in the Pt/CeO_2 samples might also give rise to detrimental effects in the reactivity of this system. Due to the large nanoparticle sizes available in the Pt/CeO_2 and Pt/SiO_2 samples, we will exclude these samples from the comparative discussion of the support effects.

The remaining samples (Pt/ZrO_2, Pt/Al_2O_3, and Pt/TiO_2) all have similar size distributions of ~8–9 nm. For these three samples the Pt/ZrO_2 is clearly the most active for the decomposition of MeOH and a support-dependence for this reaction might be inferred. It is interesting to note that the Pt/ZrO_2 and Pt/Al_2O_3 are more active than the Pt/TiO_2, suggesting that irreducible supports may be of advantage for this reaction. In a study done by Ivanov et al. [25] on the electronic state of Pt supported on different oxides, using diffuse reflectance IRS and CO as a probe molecule, it was found that Pt/ZrO_2 revealed absorption bands characteristic of CO complexes with Lewis acid sites on the surface of ZrO_2. In the same study no such features were observed for Pt/TiO_2, Pt/Al_2O_3, or Pt/SiO_2. It has also been found, in a study of MeOH adsorption and dissociation over SnO_2, that the dissociation

of MeOH to methoxide occurs preferentially at Sn^{2+} cationic sites. Therefore, acidic sites on the surface of the Pt/ZrO_2 sample may account for its superior performance relative to the other samples.

4 Conclusion

We have investigated the decomposition of MeOH over Pt deposited on various oxide supports. The samples obtained may be roughly grouped into categories consisting of large ($\sim$15–18 nm) and small ($\sim$8–9 nm) Pt particles deposited on *reducible* (CeO_2, TiO_2) and *non-reducible* (SiO_2, ZrO_2, Al_2O_3) supports. For all Pt/oxide samples tested the reaction proceeds mainly through the direct decomposition of MeOH. For the large particles deposited on highly reducible CeO_2, as well as non-reducible SiO_2, the Pt/CeO_2 is clearly more active. For these two samples, the superior performance of the Pt/CeO_2 sample can be related to the relative performances of the Pt-free supports themselves. However, for the smaller particles, deposited on TiO_2, ZrO_2, and Al_2O_3, the Pt/ZrO_2 is the most active, much more so than the Pt/TiO_2 which reaches 50% conversion at $\sim$230 °C as compared to $\sim$195 °C for the Pt/ZrO_2. The Pt/ZrO_2 is also cationic as opposed to the mainly metallic Pt on TiO_2 and Al_2O_3. Further, our XPS data indicate that for similarly sized particles the state of oxidation of Pt depends on the support. Because all samples underwent identical thermal treatments, we may conclude that the stability of $Pt^{\delta+}$ species can be affected by the choice of support. These data suggest that for MeOH decomposition, or perhaps in general, for reactions not involving the dissociation of O_2, the reducibility of the support plays a secondary role to the more important parameters of particle size and oxidation state of Pt. The role of the support is that of a stabilizer, a provider of preferential/additional sites of interaction, and a mediator among the different oxides of Pt.

Acknowledgments We gratefully acknowledge the support of this work by the Donors of the American Chemical Society Petroleum Research Fund under Grant PRF-42701-G5 and supplement for minority undergraduate summer research, and the National Science Foundation (NSF-CAREER award, No. 0448491).

References

1. Tabatabaei J, Sakakini BH, Waugh KC (2006) Catal Lett 110:77
2. Olah GA (2004) Catal Lett 93:1
3. Spencer MS (2003) Top Catal 22:135
4. Shishido T, Sameshima H, Takehira K (2003) Top Catal 22:261
5. ZumMallen M, Schmidt LD (1996) J Catal 161:230
6. Panja C, Saliba N, Koel BE (1998) Surf Sci 395:248
7. Yang Y, McElwee-White L (2004) Dalton Trans 2352
8. Cao D, Lu GQ, Wieckowski A, Wasileski SA, Neurock M (2005) J Phys Chem B 109:11622
9. Tong YY, Kim HS, Babu PK, Wazczuk P, Wiekowski A, Oldfield E (2002) J Am Chem Soc 124:468
10. Ferreira PJ, la O' GJ, Shao-Horn Y, Morgan D, Makharia R, Kocha S, Gasteiger HA (2005) J Electrochem Soc 152:A2256
11. Hendriksen BLM, Frenken JWM (2002) Phys Rev Lett 89:046101
12. Dam VAT, de Bruijn FA (2007) J Electrochem Soc 154:B494
13. Hull R, Li L, Xing Y, Chusuei CC (2006) Chem Mater 18:1780
14. Gasteiger HA, Kocha SS, Sompalli B, Wagner FT (2005) Appl Catal Environ B 56:9
15. Croy J, Mostafa S, Liu J, Sohn Y, Roldan Cuenya B (2007) Catal Lett DOI: 10.1007/S10562-007-9162-1, in press
16. Haruta M (2002) CATTECH 6:102
17. Men Y, Gnaser H, Zapf R, Hessel V, Ziegler C (2004) Catal Comm 5:671
18. Kurtz M, Strunk J, Hinrichsen O, Muhler M, Fink K, Meyer B, Wöll Ch (2005) Angew Chem Int 44:2790
19. Dellwig T, Hartmann J, Libuda J, Meusel I, Rupprechter G, Unterhalt H, Freund HJ (2000) J Mol Catal A 162:51
20. Hardacre C, Ormerod RM, Lambert RM (1994) J Phys Chem 98:10901
21. Badri A, Binet C, Lavalley JC (1996) J Chem Soc Faraday Trans 92:1603
22. Powell BR, Whittington SE (1983) J Catal 81:382
23. Sun HP, Pan XP, Graham GW, Jen HW, McCabe RW, Thevuthasan S, Peden CHF (2005) Appl Phys Lett 87:201915
24. Dulub O, Hebenstreit W, Diebold U (2000) Phys Rev Lett 84:3646
25. Ivanov AV, Kustov LM (1998) Russ Chem Bull 47:1061
26. Spatz JP, Mossmer S, Hartmann C, Moller M, Herzog T, Krieger M, Boyen HG, Ziemann P, Kabius B (2000) Langmuir 16:407
27. Roldan Cuenya B, Baeck SH, Jaramillo TF, McFarland EW (2003) J Am Chem Soc 125:12929
28. Ono LK, Sudfeld D, Roldan Cuenya B (2006) Surf Sci 600:5041
29. Bond GC, Flamerz S (1989) Appl Catal 46:89
30. Sena Y, Dogu G, Dogu T (2006) Catal Today 117:271
31. Corro G, Fierro JLG, Odilon VC (2003) Catal Commun 4:371
32. Miller ML, Linton RW (1985) Anal Chem 57:2314
33. Hughes AE, Sexton BA (1990) J Electron Spectrosc 50:15
34. Lee SA, Park KW, Choi JH, Kwon BK, Sung YE (2002) J Electrochem Soc 149:1299
35. Perrichon V, Retailleau L, Bazin P, Daturi M, Lavalley JC (2004) Appl Catal A 260:1
36. Penner S, Wang D, Podloucky R, Schlogl R, Hayek K (2004) Phys Chem Chem Phys 6:5244
37. Tang J, Lawrence JM, Hemminger JC
38. Chen M, Schmidt LD (1978) J Catal 55:348
39. Silvestre-Albero J, Sepulveda-Escribano A, Rodriguez-Reinoso F, Anderson JA (2004) J Catal 223:179
40. Laursen S, Linic S (2006) Phys Rev Lett 97:026101
41. Bjorneholm O, Federmann F, Fossing F, Moller T (1995) Phys Rev Lett 74:3017
42. Fu Q, Saltsburg H, Flytzani-Stephanopoulos M (2003) Science 301:935
43. Matsumura Y, Okumura M, Usami Y, Kagawa K, Yamashita H, Anpo M, Haruta M (1997) Catal Lett 44:189
44. Usami Y, Kagawa K, Kawazoe M, Matsumura Y, Sakurai H, Haruta M (1998) Appl Catal A 171:123
45. Lopez N, Janssens TVW, Clausen BS, Xu Y, Mavrikakis M, Bligaard T, Norskov JK (2004) J Catal 223:232
46. Imamura S, Hagashihara T, Saito Y, Aritani H, Kanai H, Matsumura Y, Tsuda N (1999) Catal Today 50:369